Supplementary material for

Novel intramolecular-tailored g-C_3N_4 with accelerated charge delivery for photocatalytic tetracycline degradation and hydrogen production: Experimental studies and theoretical analyses

Yating Wang[a,], Chaosheng Peng[a], Airu Liu[a], Jinyue Song[a], Xingang Li[b], Tao Jiang[a,]**

[a]Tianjin Key Laboratory of Brine Chemical Engineering and Resource Eco-utilization, School of Chemical Engineering and Material Science, Tianjin University of Science & Technology, Tianjin 300457, P. R. China.

[b]Collaborative Innovation Center of Chemical Science and Engineering (Tianjin), Tianjin Key Laboratory of Applied Catalysis Science & Engineering, School of Chemical Engineering & Technology, Tianjin University, Tianjin 300072, P. R. China.

*Corresponding author. E-mail: wangyating@tust.edu.cn (Yating Wang); jiangtao@tust.edu.cn (Tao Jiang)

The apparent quantum efficiency (AQE)

The apparent quantum efficiency (AQE) of photocatalytic water splitting for hydrogen evolution was conducted under similar condition. The light source is a Xe lamp with 400 nm bandpass filter, and the test time is 1 h. The AQE is calculated according to the following equation[1].

$$AQE(\%) = \frac{Number\ of\ reacted\ electrons}{Number\ of\ incident\ photons} \times 100 = \frac{2MN_A hc}{AIt\lambda} \times 100 \quad (1)$$

where M, N_A, h and c represent the number of hydrogen molecules, Avogadro's constant, Planck constant and light velocity, respectively. The total number of incident photons was measured using a PM100D power meter (Thorlabs, America). A is the irradiation area (36.3 cm^2).

The degradation efficiency (DE)

The degradation efficiency (DE) of TC could be calculated by the following equation (1):

$$DE\ \% = (C_0 - C_t)/C_0 \times 100 \quad (2)$$

where C_0 and C_t are the initial and containing concentration of tetracycline after several regular intervals of time (t), respectively. Furthermore, the reaction kinetic properties were calculated by pseudo-first-order kinetics based on the following equation (2):

$$\ln(C_0/C_t) = k_{app}t \quad (3)$$

where the slope k_{app} (min^{-1}) and t (min) are the apparent rate constant and reaction time, respectively.

The conduction band bottom (CBM) position

The flat-band potentials measured from the Ag/AgCl standard electrode were converted to flat-band potentials with respect to the standard hydrogen electrode potential (NHE) by equation of the flat-band potential [8]:

$$E_{fb\ (vs.\ NHE)} = E_{fb\ (pH=0,\ vs.\ Ag/AgCl)} + E_{AgCl} + 0.059 \times pH \quad (4)$$

For n-type semiconductors, E_{fb} about 0.3 V lower than its conduction band (CB) position.

Computational methods

All the calculations were performed within the framework of the density functional theory (DFT) as implemented in the Vienna Ab initio Software Package (VASP 5.4.4) code within the Perdew–Burke–Ernzerhof (PBE) generalized gradient approximation and the projected augmented wave (PAW) method [2-5]. The cutoff energy for the plane-wave basis set was set to 450 eV. The Brillouin zone of the surface unit cell was sampled by Monkhorst–Pack (MP) grids, with a k-point mesh for g-C_3N_4 and CH_3CH_2-g-C_3N_4 structures optimizations [6]. The g-C_3N_4 and CH_3CH_2-g-C_3N_4 structures structures were determined by 3 × 3 × 1 Monkhorst-Pack grid. The convergence criterion for the electronic self-consistent iteration and force was set to 10^{-5} eV and 0.01 eV/Å, respectively. A 12 Å vacuum was introduced to avoid interactions between periodic images. HSE06 method was used with following standard parameters: $\alpha = 0.25$ and $\omega = 0.20$, which work well in terms of correcting the band gaps of common semiconductors.

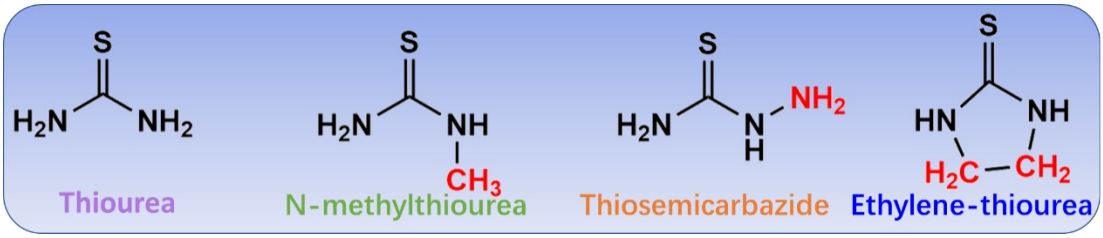

Fig. S1 Molecular structure of Thiourea, N-methylthiourea, Thiosemicarbazide and Ethylene-thiourea.

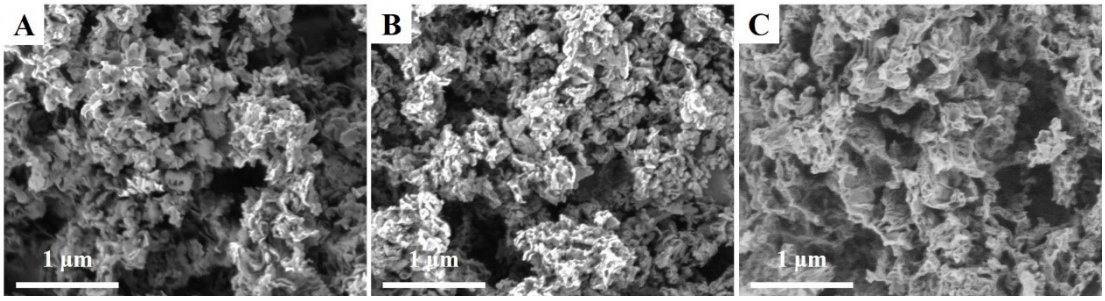

Fig. S2 SEM images of (A) CN-E-0, (B) CN-E-75 and (C) CN-E-300

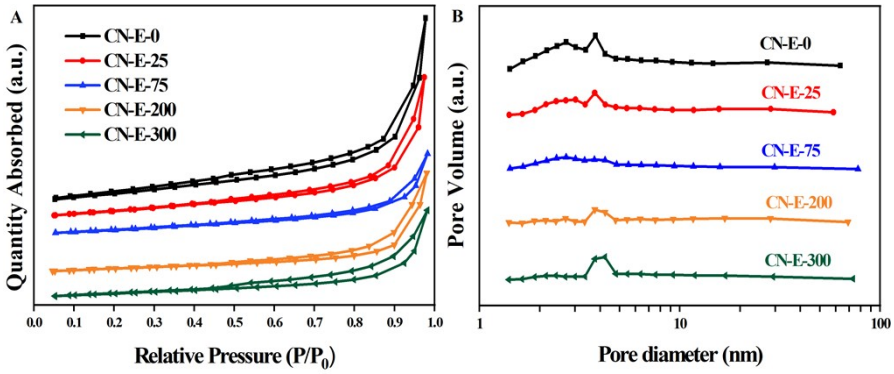

Fig. S3 (A) N_2 adsorption-desorption isotherms and (B) Corresponding pore size distribution curves of CN-E-X.

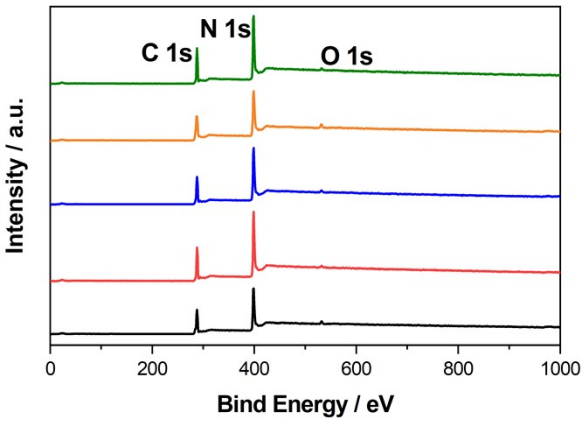

Fig. S4 XPS survey spectra of CN-E-X

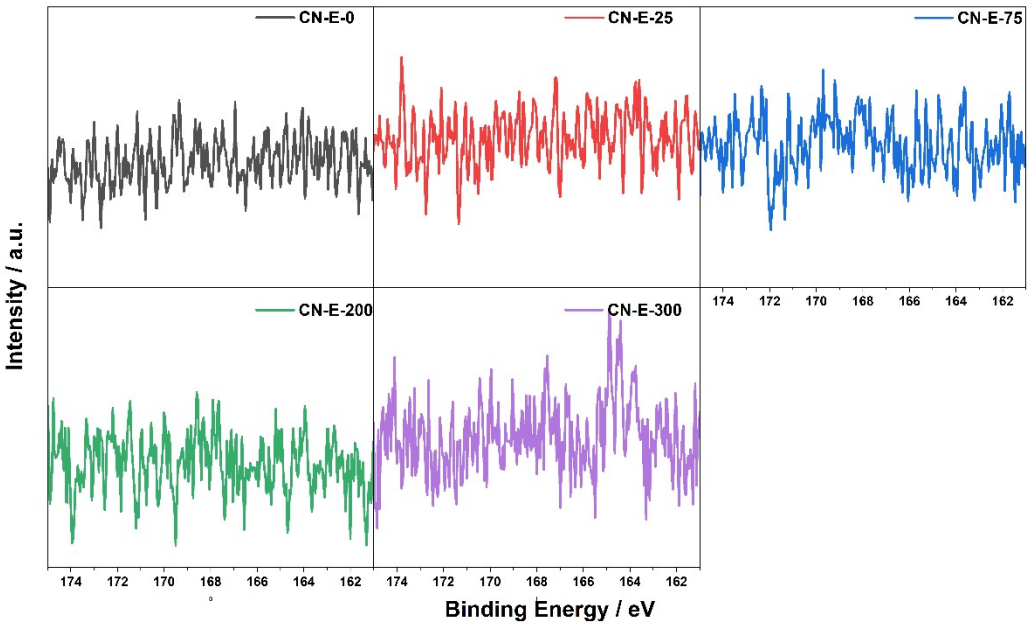

Fig. S5 S 2p XPS spectra of CN-E-X.

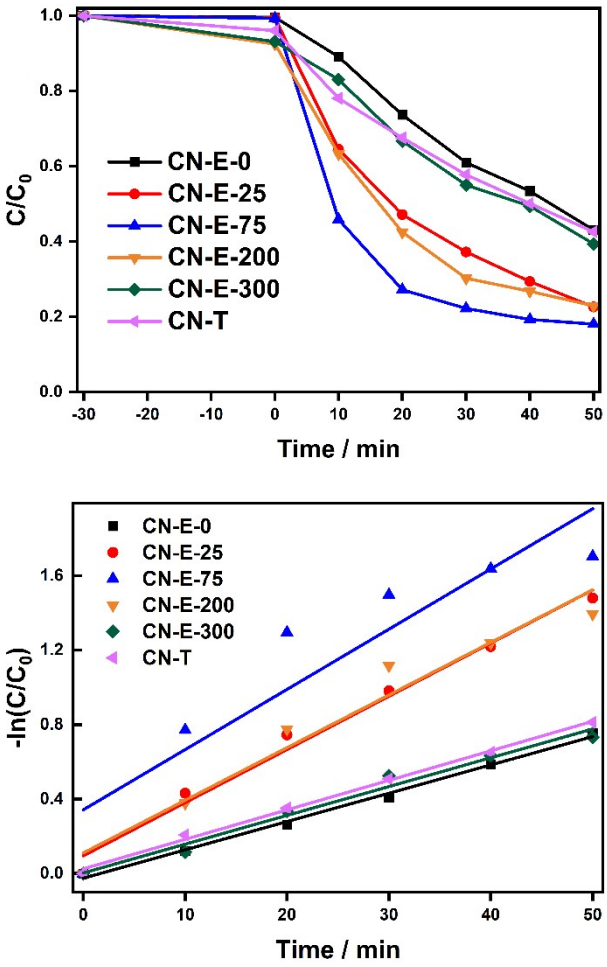

Fig. S6 (A) The photocatalytic degradation of TC by CN-E-X and CN-T under visible light irradiation (including the dark reaction stage); (B) The kinetic data drawing by $\ln(C_0/C) = k_{app}\, t$

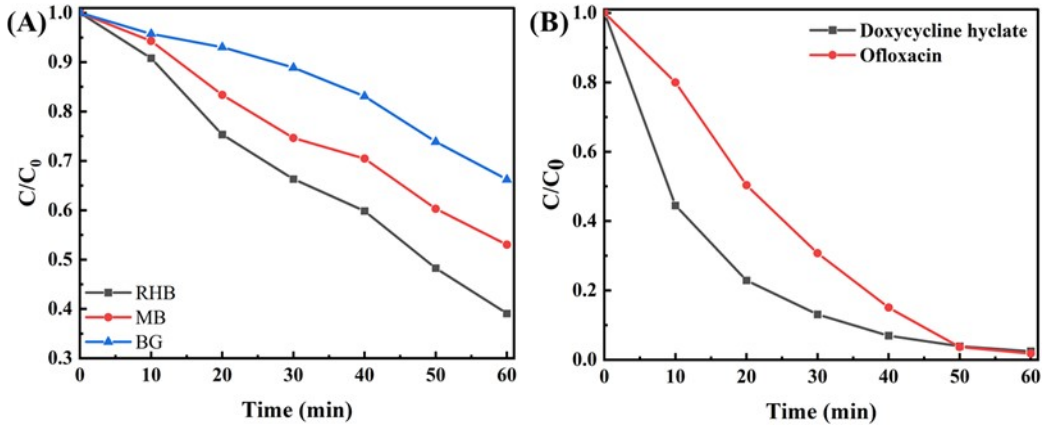

Figure S7 The photocatalytic degradation of (A) different dyes and (B) different antibiotics by CN-E-75 under visible light irradiation.

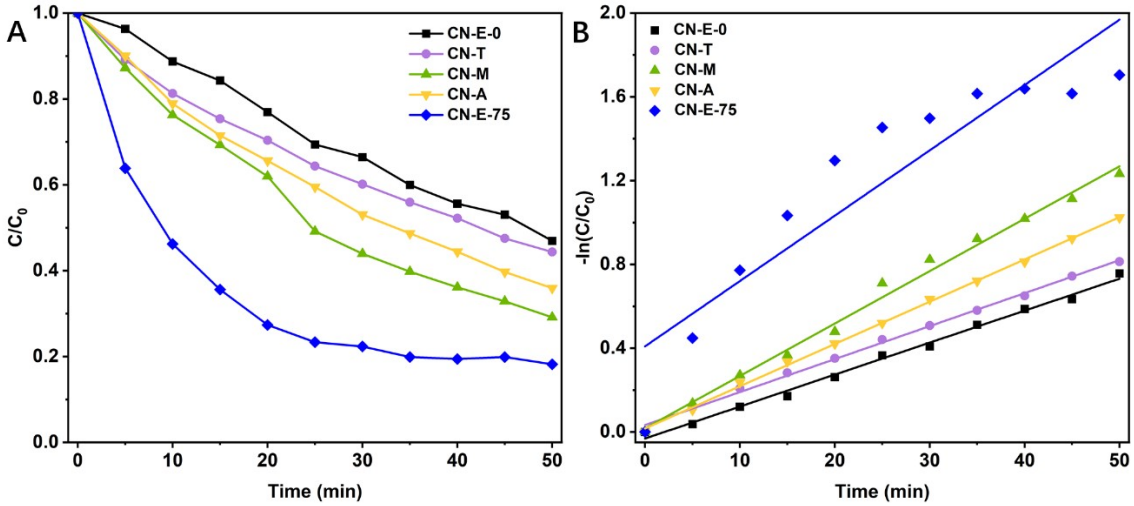

Fig. S8 (A) The photocatalytic degradation of TC under visible light irradiation and (B) the kinetic data drawing of CN-E-0, CN-T, CN-M, CN-A, and CN-E-75.

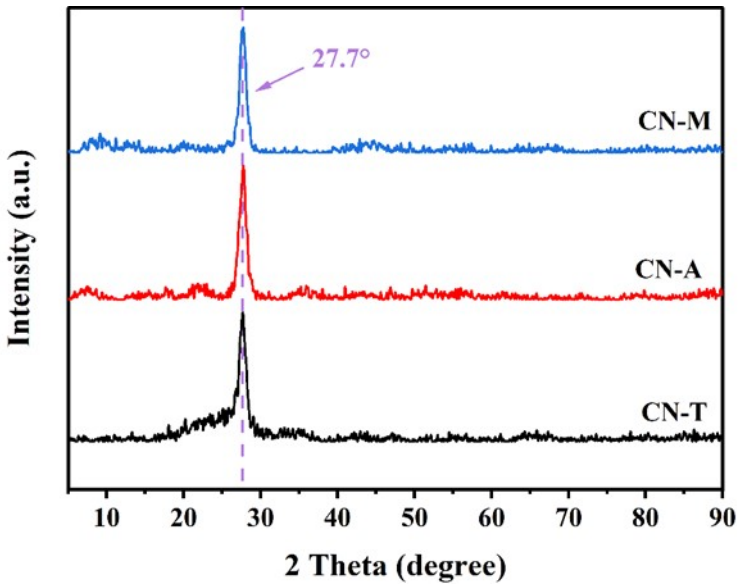

Figure S9 XRD patterns of CN-T, CN-A and CN-M.

From the XRD spectra, the planar structure of the thiourea modified g-C_3N_4 (CN-T), N-methylthiourea modified g-C_3N_4 (CN-M), thiosemicarbazide modified g-C_3N_4 (CN-A) were disrupted due to the weakening of the peak intensity at the (100) crystal plane located at 13 ˚. In addition, unlike CN-E-75, the peak of CN-T, CN-A, CN-M representing interlayer stacking did not shift left, indicating that the layer spacing did not change significantly.

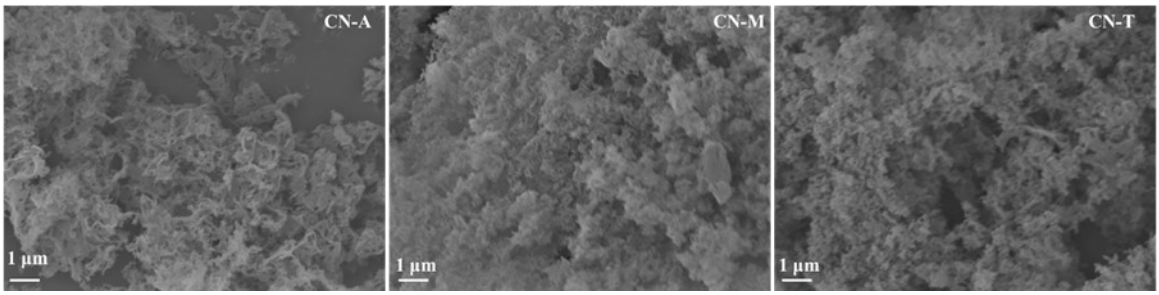

Figure S10 SEM of CN-A, CN-M, and CN-T.

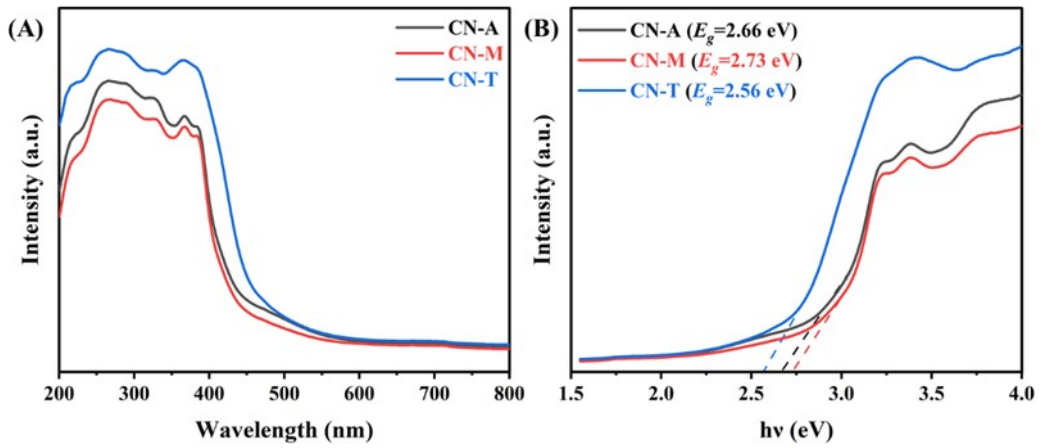

Figure S11 (A) UV-vis DRS and (B) the corresponding Kubelka-Munk transformed diffuse reflectance of CN-A, CN-M, CN-T.

The UV-vis absorption spectra do not differ much from that of pure carbon nitride CN-E-0. The absorption edge of CN-T is greater than CN-E-0 but less than CN-E-75. Namely, for equimolar amounts of thiourea, N-methylthiourea, thiosemicarbazide and ethyl-thiourea modified carbon nitride CN-T, CN-M, CN-A, and CN-E-75, the ethyl-thiourea modified CN-E-75 showed stronger light absorption in the whole wavelength range. Therefore, we believe that higher light absorbance and changed layer spacing may be responsible for significantly more strengthen activity of ethyl-modified g-C_3N_4 (CN-E-75).

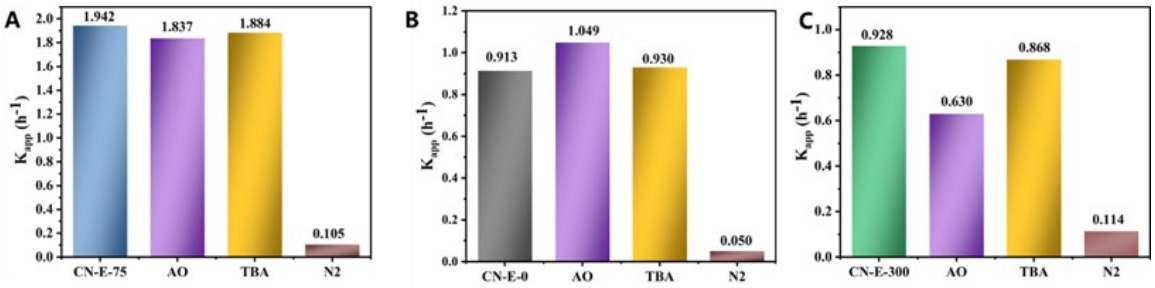

Figure S12 The Kapp of photo-degradation of TC over (A) CN-E-75, (B) CN-E-0, and (C) CN-E-300 with different radical scavengers.

Table S1 The physicochemical properties of CN-E-X.

samples	BET surface area (m^2/g)	Pore Diameter (nm)	Pore volume (cm^3/g)
CN-E-0	160.90	3.785	0.518
CN-E-25	128.07	3.762	0.394
CN-E-75	87.28	2.707	0.230
CN-E-200	70.76	3.767	0.275
CN-E-300	67.14	4.224	0.247

Table S2 The quantitative elemental analysis from XPS of CN-E-X

sample	C (at. %)	N (at. %)	O (at. %)	C/N
CN-E-0	43.73	54.33	2.04	0.80
CN-E-25	41.95	56.58	1.47	0.74
CN-E-75	43.16	54.81	2.03	0.79
CN-E-200	46.16	50.96	2.88	0.91
CN-E-300	49.84	46.37	3.79	1.07

Table S3 The elemental analysis from EA of CN-E-X

sample	C (at. %)	N (at. %)	H (at. %)	C/N
CN-E-0	35.78	62.68	1.51	0.66
CN-E-25	35.61	62.08	1.49	0.67
CN-E-75	34.90	59.45	1.79	0.68
CN-E-200	35.43	52.52	2.12	0.79
CN-E-300	36.64	51.12	2.15	0.84

Table S4. The peak position and relative proportions of N species in N1s spectra of the samples.

Samples	Peak position (eV)			Peak area ratio (%)		
	N_{2C}	N_{3C}	$N_{C\text{-}N\text{-}H}$	N_{2C}	N_{3C}	$N_{C\text{-}N\text{-}H}$
CN-E-0	398.6	399.7	400.9	73.7	13.9	12.4
CN-E-25	398.6	399.7	400.9	68.8	18.7	12.5
CN-E-75	398.6	399.6	400.9	67.7	19.2	13.1
CN-E-200	398.5	399.8	400.9	63.5	21.4	15.1
CN-E-300	398.6	399.8	401.0	62.1	21.6	16.3

Table S5. The peak position and relative proportions of C species in C1s spectra of the samples.

Samples	Peak position (eV)		Peak area ratio (%)	
	C_N	C_C	C_N	C_C
CN-E-0	288.1	284.7	87.6	12.4
CN-E-25	288.1	284.7	96.3	3.7
CN-E-75	288.1	284.7	91.4	8.6
CN-E-200	287.7	284.9	84.3	15.7
CN-E-300	288.1	284.9	72.7	27.3

Table S6. Kinetic constants extracted from the photoluminescence decay profiles of CN-E-X

Samples	τ_1(ns)	A_1 (%)	τ_2(ns)	A_2 (%)	τ_{ave} (ns)	$R^{2(a)}$
CN-E-0	1.057	82.2	6.414	17.8	4.01	0.996
CN-E-25	0.873	80.6	4.407	19.4	2.81	0.997
CN-E-75	0.703	88.7	3.463	11.3	1.76	0.995
CN-E-200	0.506	86.2	1.803	13.8	0.97	0.962
CN-E-300	0.273	74.1	0.599	25.9	0.41	0.969

(a) correlation coefficient

The time-resolved fluorescence decay curves of samples are proved by biexponential fitting equation[7]:

$$I(t) = y_0 + A_1 \times \exp\left(\frac{-t}{\tau_1}\right) + A_2 \times exp(\frac{-t}{\tau_2}) \quad (5)$$

$$\tau_{ave} = \frac{A_1\tau_1^2 + A_2\tau_2^2}{A_1\tau_1 + A_2\tau_2} \quad (6)$$

A_1 and A_2 are constants and can be obtained by direct fitting from the decay curves. τ_1 and τ_2 are the fast decay life and slow decay life of the fitted results, respectively.

Table S7. The k_{app} and the linear fitting correlation coefficient R^2 for CN-E-X determined.

Samples	$R^{2(a)}$	k_{app} (min^{-1})
CN-E-0	0.994	0.0152
CN-E-25	0.982	0.0286
CN-E-75	0.813	0.0323
CN-E-200	0.945	0.0283
CN-E-300	0.977	0.0154
CN-T	0.996	0.0158

(a) linear fitting correlation coefficient

Table S8 The comparison of photocatalytic H_2 evolution rate over reported g-C_3N_4-based photocatalysts

Samples	Light sources	Co-catal.	T (ºC)	Reactant solution	HER (μmol/g·h)	Ref.
CN-E-75	**Xe lamp (λ > 400 nm)**	**3 wt. % Pt**	**5**	**100 mL, 20 % triethanolamine**	**1150**	**This work**
DACN	Xe lamp (λ > 420 nm)	3 wt. % Pt	5	100 mL, 10 % triethanolamine	595	Appl. Surf. Sci. 2021, 560, 150029
ODCN	Xe lamp (λ > 420 nm)	3 wt. % Pt	5	100 mL, 10 % triethanolamine	364	New J Chem. 2021, 44, 16320-16328
g-C_3N_4 NS	300 W Xe lamp (λ≥420	3 wt. % Pt	5	100 mL distilled water	101.4	Nano Energy. 2019, 59, 644-650
SSCN	300 W Xe lamp (λ≥420 nm)	3 wt. % Pt	10	100 mL, 15 % triethanolamine	496	Small. 2016, 26, ,3543-3549
CNU0.075	300 W Xe lamp (λ≥500 nm)	3 wt. % Pt	5	100 mL, 10 % triethanolamine	94.1	Appl. Catal. B: Environ. 2019, 254, 128–134
CCN-1	300 W Xe lamp (λ≥420 nm)	3 wt. % Pt	10	100 mL, 10 % triethanolamine	529	Appl. Catal. B: Environ. 2019, 229, 114–120
g-C_3N_{4+x}	300 W Xe lamp (λ≥400 nm)	3 wt. % Pt	5	100 mL, 10 % triethanolamine	557	J. Mater. Chem. A 2015, 26, .13819-13826
CCN-550	300 W Xe lamp (λ≥420 nm)	3 wt. % Pt	20	100 mL, 10 % methanol	330	Appl. Catal. B: Environ. 2018, 231, 234-241
CNO-96	300 W Xe lamp (λ≥400 nm)	3 wt. % Pt	7	100 mL, 10 % triethanolamine	264	Appl. Catal. B: Environ. 2017, 206, 417-425
P10-550	300 W Xe lamp (λ > 420 nm)	3 wt. % Pt	5	100 mL, 10 % triethanolamine	506	J. Mater. Chem. A 2015, 3, 3862-3867

Reference

[1] X. Yan, B. Xu, X. Yang, J. Wei, B. Yang, L. Zhao, G. Yang, Through hydrogen spillover to fabricate novel 3DOM-H$_x$WO$_3$/Pt/CdS Z-scheme heterojunctions for enhanced photocatalytic hydrogen evolution, Appl. Catal. B Environ. 256 (2019) 117812.

[2] J.P. Perdew, K. Burke, M. Ernzerhof, Generalized gradient approximation made simple, Phys. Rev. Lett. 77 (1996) 3865-3868.

[3] B. Hammer, L.B. Hansen, J.K. Nørskov, Improved adsorption energetics within density-functional theory using revised perdew-burke-ernzerhof functionals, Phys. Rev. B 59 (1999) 7413-7421.

[4] P.E. Blöchl, Projector augmented-wave method, Phys. Rev. B 50 (1994) 17953-17979.

[5] G. Kresse, D. Joubert, From ultrasoft pseudopotentials to the projector augmented-wave method, Phys. Rev. B 59 (1999) 1758-1775.

[6] H.J. Monkhorst, J.D. Pack, Special points for brillouin-zone integrations, Phys. Rev. B 13 (1976) 5188-5192.

[7] G. Zhang, G. Li, Z.A. Lan, L. Lin, A. Savateev, T. Heil, S. Zafeiratos, X. Wang, M. Antonietti, Optimizing optical absorption, exciton dissociation, and charge transfer of a polymeric carbon nitride with ultrahigh solar hydrogen production activity, Angew Chem. Int. Ed. Engl. 56 (2017) 13445-13449.

[8] Y. Wang, C. Peng, T. Jiang, J. Zhang, Z. Jiang, X. Li, Construction of defect-engineered three-dimensionally ordered macroporous WO_3 for efficient photocatalytic water oxidation reaction, J. Mater. Chem. A 9 (2021) 3036-3043.